December 17, 2014
Preprint typeset using LaTeX style emulateapj v. 5/2/11

arXiv:1412.5444v1 [astro-ph.GA] 17 Dec 2014

THE RINGS SURVEY I: Hα AND H I VELOCITY MAPS OF GALAXY NGC 2280[1]

Carl J. Mitchell, T. B. Williams[2,3]
Department of Physics and Astronomy, Rutgers University and
136 Frelinghuysen Road, Piscataway, NJ 08854

Kristine Spekkens, K. Lee-Waddell
Department of Physics, Royal Military College of Canada and
P.O. Box 17000, Station Forces, Kingston, ON, K7K 7B4, XNS, Canada

Rachel Kuzio de Naray
Department of Physics and Astronomy, Georgia State University and
25 Park Place, Atlanta, GA 30303

and

J. A. Sellwood
Department of Physics and Astronomy, Rutgers University and
136 Frelinghuysen Road, Piscataway, NJ 08854

December 17, 2014

ABSTRACT

Precise measurements of gas kinematics in the disk of a spiral galaxy can be used to estimate its mass distribution. The Southern African Large Telescope (SALT) has a large collecting area and field of view, and is equipped with a Fabry-Pérot interferometer that can measure gas kinematics in a galaxy from the Hα line. To take advantage of this capability, we have constructed a sample of 19 nearby spiral galaxies, the RSS Imaging and Spectroscopy Nearby Galaxy Survey (RINGS), as targets for detailed study of their mass distributions and have collected much of the needed data. In this paper, we present velocity maps produced from Hα Fabry-Pérot interferometry and H I aperture synthesis for one of these galaxies, NGC 2280, and show that the two velocity measurements are generally in excellent agreement. Minor differences can mostly be attributed to the different spatial distributions of the excited and neutral gas in this galaxy, but we do detect some anomalous velocities in our Hα velocity map of the kind that have previously been detected in other galaxies. Models produced from our two velocity maps agree well with each other and our estimates of the systemic velocity and projection angles confirm previous measurements of these quantities for NGC 2280.

Subject headings: galaxies: individual: NGC 2280, galaxies: kinematics and dynamics

1. INTRODUCTION

The centrifugal balance of gas moving at close to the circular speed in the plane of a disk galaxy offers a direct estimate of the central gravitational attraction, and therefore a means to estimate the distribution of mass within the galaxy (Öpik 1922; Roberts 1969; Tully & Fisher 1977). The general flatness of spiral galaxy rotation curves at large radii (Babcock 1939; Rubin *et al.* 1980; Bosma 1981) provides some of the strongest evidence for extended halos of dark matter (hereafter DM).

The standard Lambda Cold Dark Matter (ΛCDM) cosmological paradigm is a highly successful model for the growth of structure in the universe, particularly on large scales (Springel *et al.* 2006). However, it is not yet clear whether galaxy formation within the ΛCDM framework can produce systems whose underlying structure matches that observed. The clearest galaxy-scale prediction from the ΛCDM model is the expected density profile of the DM halo, which was first believed to have a simple broken power law form (Navarro *et al.* 1996). However, a profile with a slope that decreases continuously inwards from the break radius, where $\rho \propto r^{-2}$, and a central density that is large but finite (Einasto & Haud 1989), appears to be a better fit in DM only models (Navarro *et al.* 2004, 2010; Merritt *et al.* 2005; Gao *et al.* 2008).

Galaxies are believed to form in the DM halos as gas collects, cools, and settles into rotational balance (White & Rees 1978; Fall & Efstathiou 1980; Gunn 1982; Kereš *et al.* 2005; Dekel & Birnboim 2006). The extra central attraction of the baryons in the inner parts causes the DM halo to contract adiabatically, increasing its inner density (Blumenthal *et al.* 1986; Gnedin *et al.* 2004; Sellwood & McGaugh 2005). Furthermore, bursts of star formation may release sufficient energy into the gas to cause it to expand out of the proto-disk, and perhaps right out of the halo, on a short time-scale. Sim-

cmitchell@physics.rutgers.edu
williams@saao.ac.za
kristine.spekkens@rmc.ca
karen.lee-waddell@rmc.ca
kuzio@astro.gsu.edu
sellwood@physics.rutgers.edu

[1] Based in part on observations obtained with the Southern African Large Telescope (SALT) programme 2011-3-RU-003

[2] South African Astronomical Observatory, Observatory, Cape Town 7925, South Africa
[3] Astronomy Department, University of Cape Town, Rondebosch 7700, South Africa

ulations of forming galaxies that include a higher density threshold for star formation (*e.g.,* Governato *et al.* 2010) manifest repeated non-adiabatic changes in the disk mass that can cause the halo density to decrease (*e.g.,* Read & Gilmore 2005; Pontzen & Governato 2012) in models of dwarf galaxies, but are less effective at higher masses (Brook *et al.* 2011; Guedes *et al.* 2011; DiCinto *et al.* 2014; Pontzen & Governato 2014).

Rotation curve measurements of spiral galaxies can, in principle, test these gradually evolving predictions for the mass distribution. However, a one-dimensional rotation curve does not contain sufficient information to measure the separate distributions of dark and visible matter (van Albada *et al.* 1985; Sackett 1997). No consensus has yet emerged on the best way to separate the contributions of the stellar components from that of the dark matter, *e.g.,* Weiner *et al.* (2001) and Bershady *et al.* (2011) reach widely differing conclusions. However, near maximal disks embedded in lower density halos are favored by a number of theoretical arguments, such as spiral-arm multiplicities (Sellwood & Carlberg 1984; Athanassoula *et al.* 1987) and bar-halo friction (Debattista & Sellwood 2000).

As the baryonic mass in dwarf and low surface brightness galaxies is believed to be a much smaller fraction of the total than in Milky Way size galaxies, the rotation curve yields a more direct measure of the DM halo density. Various authors (*e.g.,* Rhee *et al.* 2004; Hayashi *et al.* 2006; Valenzuela *et al.* 2007) have raised a number of potential biases in such measurements, such as non-circular motions, pressure and projection effects, and halo triaxiality that need to be taken into account when deriving the DM density profile. These difficulties can be overcome with good two-dimensional data, and Kuzio de Naray & Spekkens (2011) find that the DM density remains lower than predicted; baryonic processes have helped to ease the tension (*e.g.,* Oh *et al.* 2011; Governato *et al.* 2012) but have not eliminated it. Other studies of the rotation curves of generally more massive spiral galaxies (*e.g.,* McGaugh *et al.* 2007) also suggest lower, and more uniform, halo densities in the inner parts than predicted in ΛCDM models. In fact, Dutton *et al.* (2007) suggest that the only way to reconcile the predictions with the measured rotation curves of larger galaxies is to invoke an unexplained de-compression of the DM halo as the baryons settle to the center.

In order to address all these issues, we clearly require yet higher quality measurements of velocities over the projected disks of moderately inclined spiral galaxies. Ideally, such measurements should have the spatial resolution to determine the inner density and extend to large enough radii to constrain the break radius of the halo density profile. Two-dimensional velocity maps are needed in order to reveal non-axisymmetric flow patterns that could be missed in longslit data, and modeling such flow patterns leads to improved estimates of the mean interior density (Spekkens & Sellwood 2007).

The 11m Southern African Large Telescope (SALT) has a similar design to the Hobby-Eberly telescope (Sebring & Ramsey 1997). The Robert Stobie spectrogaph (RSS) on SALT (Buckley *et al.* 2006) is equipped with a Fabry-Pérot spectrophotometer (hereafter FP) that can measure the Doppler shift of emission lines over the full 8 arcmin field of view. A detailed overview of the SALT RSS Fabry-Pérot instrument is provided by Rangwala *et al.* (2008).

To take advantage of the large collecting area and field of view of SALT, we have designed RINGS, the RSS Imaging and Spectroscopy Nearby Galaxy Survey, that seeks to obtain detailed velocity maps at optical spatial resolution over this large field of view for 19 nearby spiral galaxies.

A number of previous surveys have obtained two-dimensional velocity maps of nearby galaxies with similar goals to those of our RINGS program: *e.g.,*, Schommer *et al.* (1993), BHαBAR (Hernandez *et al.* 2005), GHASP (Epinat *et al.* 2008), GHαFAS (Hernandez *et al.* 2008), and DiskMass (Bershady *et al.* 2010). However, they had differing target selection criteria, employed a variety of instrumental strategies and data analysis methods, and were carried out on telescopes with apertures ranging from 1.5-m to 4.2-m. Some used optical spectroscopy only, while others combined radio and optical data.

Our RINGS program uses a Fabry-Perot interferometer having an $8'$ field of view on a 10m optical telescope to produce very deep and extensive kinematic maps with optical resolution. We complement these data with high-sensitivity, but lower spatial resolution 21-cm aperture synthesis observations that provide high-quality velocity measurements into the outskirts of the program galaxies. We also have new, deep multi-band photometry extending into the near-infrared to constrain the luminous components of the galaxies. We will analyze these data with state-of-the-art dynamical methods to produce the best possible determinations of the distribution of luminous and dark matter within the target objects. Our focus is on a relatively small sample of galaxies that nonetheless covers a broad range of morphological structures and luminosities, with an in-depth, handcrafted analysis of each galaxy that will allow us to deal fully with the unique characteristics of each individual target. Our ultimate goal is to combine all these data in order to model the mass distribution within all our program galaxies for comparison with the predictions from ΛCDM cosmology.

The purpose of this first paper is to demonstrate that the FP instrument on SALT can provide reliable velocity maps of the quality needed to accomplish the science goals of RINGS. We therefore present kinematic measurements of the Hα-line emission from excited hydrogen in one of the first galaxies from the RINGS sample to be observed with SALT, NGC 2280, and compare them with similar maps of the same galaxy obtained using Karl G. Jansky Very Large Array (VLA) observations of the 21cm line of H I. The spatial and velocity resolutions of these two instruments differ substantially, and they measure different components of the interstellar gas in the galaxy. However, in both cases the radiating gas should be a good tracer of the gravitational potential, and the measured velocities ought to agree within the estimated uncertainties. We find that this is indeed the case.

2. NGC 2280: BASIC PROPERTIES

NGC 2280 is classified as a SA(s)cd galaxy (de Vaucouleurs *et al.* 1991). Figure 1(a) shows an R-band continuum image taken with the CTIO 0.9m telescope (Kuzio de Naray *et al.*, in peparation). Lauberts & Valentijn (1989) give a value for R_{25} of

TABLE 1
Galaxies Near NGC 2280

Galaxy Designation	Angular Separation (arcmin)	Velocity Separation (km s^{-1})	Apparent R-band Magnitude[a]
ESO 427- G 005[b]	11.9	+136	15.4
ESO 427- G 004[b]	13.3	−194	15.8
AM 0643-272[c]	14.4	+304	–
ESO 490- G 035[b]	26.5	+242	13.1
ESO 490- G 036[b]	29.3	+ 39	13.6
NGC 2272[d]	30.3	+231	11.3
AM 0644-280[c]	31.6	+117	–
ESO 490- G 044[b]	33.4	+269	13.3
2MASX J06415402-2727239[e]	40.3	− 28	–
ESO 490- G 031[b]	55.4	+ 92	14.1
ESO 490- G 042[b]	56.8	−141	14.6
ESO 490- G 038[d]	59.3	+ 75	13.0

Note. — Galaxies with measured systemic velocies near that of NGC 2280 and angular separations from NGC 2280 less than 1°. At our adopted distance to NGC 2280, an angular separation of 10′ correspnds to a projected separation of 68 kpc. The R-band magnitudes are to the R_{25} isophote and that for NGC 2280 is 10.76.

[a] (Lauberts & Valentijn 1989)
[b] (Garcia *et al.* 1994)
[c] (Matthews *et al.* 1995)
[d] (Huchra *et al.* 2012)
[e] (Paturel *et al.* 2005)

380″ in the B band. Koribalski *et al.* (2004) give a heliocentric systemic velocity of $v_{\rm sys} \simeq 1899$ km s^{-1}. The galactocentric velocity of $v_{\rm gsr} \simeq 1703$ km s^{-1}, together with an adopted Hubble constant of $H_0 = 73.0$ km s^{-1} Mpc^{-1}, indicate a distance of ~ 23.3 Mpc, and thus an angular scale of 0.113 kpc arcsec^{-1}. At this distance, the apparent V-band magnitude, $m_V = 9.61$ (de Vaucouleurs *et al.* 1991), corresponds to an absolute magnitude $M_V = -22.23$. Its radio flux at 1.49 GHz is 59.7 mJy (Condon *et al.* 1996).

Arp & Madore (1987) note the existence of five apparent companion galaxies to NGC 2280. We searched NED[4] for galaxies within one degree of the center of NGC 2280 having redshifts within 500 km s^{-1} of its systemic velocity. We list these possible companion galaxies in Table 1, however we do not find significant indications of recent interactions or tidal distortions in our data.

3. Hα FABRY-PÉROT OBSERVATIONS

3.1. *Observations*

We have measured the Hα emission from the disk of NGC 2280 using the medium-resolution mode of the RSS Fabry-Pérot etalon on SALT. On each of two nights, 1 Nov. 2011 and 28 Dec. 2011, we obtained 25 one-minute exposures, covering the spectral region 6565.5Å to 6643.5Å in equally-spaced 2Å steps. In order to deal with possible drifts of the etalon wavelength calibration, we first scanned the spectral range in 4Å steps, and then filled in with exposures at interleaving spacings of the etalon.

The seeing for the nights of 1 Nov. 2011 and 28 Dec. was approximately 1.75″ and 2.0″, respectively. The pixel scale of the CCD is 0.5″.

Our observations were taken in single-etalon, medium spectral resolution mode. The RSS Fabry-Pérot system is designed to operate in dual-etalon mode, using a lower resolution etalon to reject unwanted adjacent interference orders of the medium resolution etalon (see Rangwala *et al.* 2008, for details). Unfortunately, the current mechanical support structure of the etalons in the spectrograph does not maintain their position with sufficient rigidity; misalignments introduce reflections between the two etalons that give rise to a series of strong ghost images, making dual-etalon observations impossible. Our single-etalon mode observations use only the medium resolution etalon and an interference filter. This allows not only the desired interference order to be recorded, but also two other adjacent orders transmitted by the filter. This is not a serious impediment for our measurements of emission lines, since there are no other emission features at the other transmitted wavelengths (separated by the 75 Å free spectral range of the medium resolution etalon). The galaxy continuum and the night sky continuum are however three times brighter than would be obtained from a single order, reducing the signal-to-noise achieved in our measurements. Planned mechanical modifications to the spectrograph will allow dual-etalon measurements to be made in the future.

3.2. *Photometric calibration*

We also obtained twilight sky flat-field images, taken with the interference filter but without the etalon, to correct for pixel-to-pixel gain variations in the CCD detector and for vignetting within the telescope and spectrograph. The fundamental design of SALT causes the effective collecting area of the primary mirror to vary over a track, resulting in an overall sensitivity variation of about 30%. Also, the SALT spherical aberration corrector introduces differential vignetting across the field of view that varies over the course of a track with an amplitude of approximately 5 to 10%. We use our R-band photometry of NGC 2280 obtained at the CTIO 0.9m telescope to correct for these latter two effects. We compare the photometry of

[4] `http://ned.ipac.caltech.edu`

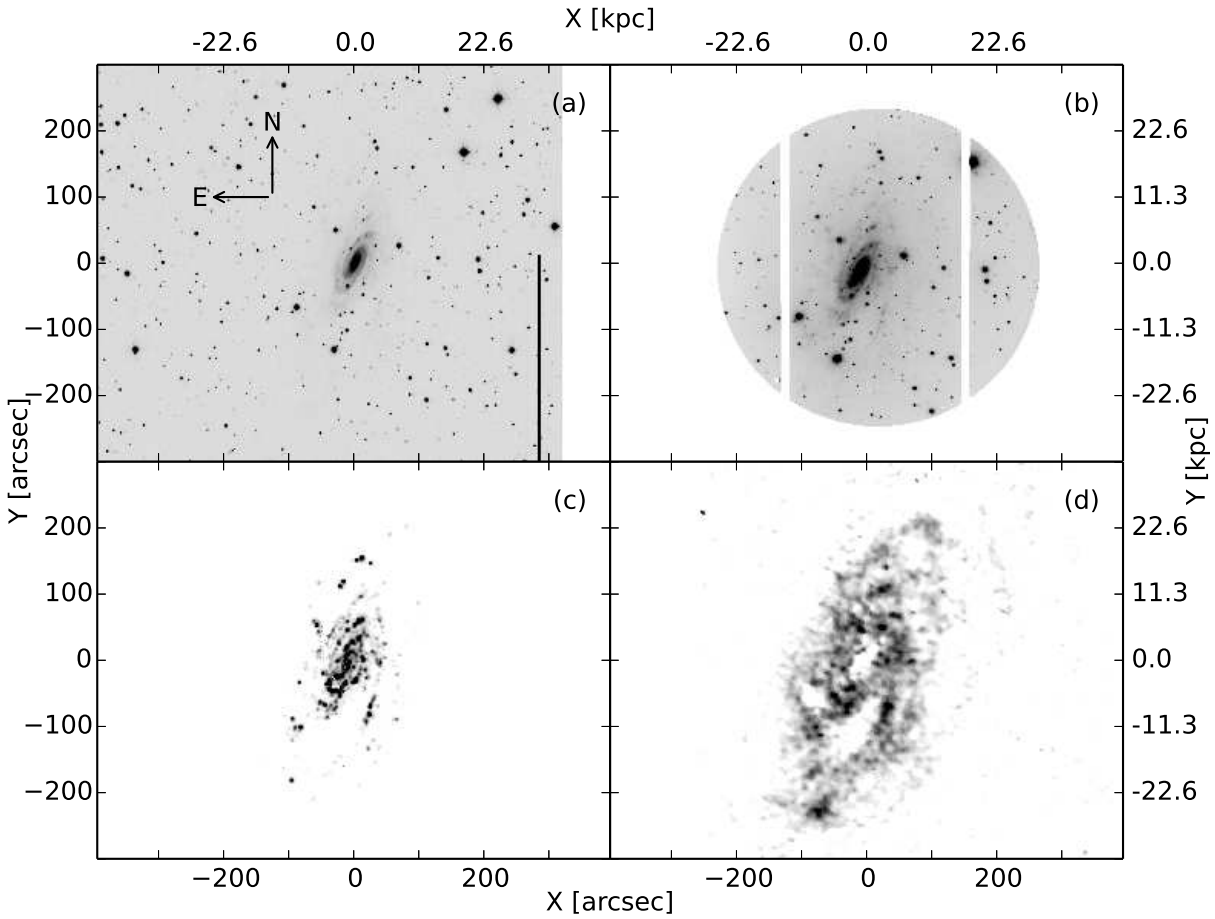


FIG. 1.— Intensity maps of NGC 2280 with the same spatial scales. (a) An R-band continuum image acquired using the CTIO 0.9 m. The indicated orientation is the same for all other panels. (b) The stacked intensity of our SALT RSS Fabry-Pérot images from 11 Nov. 2011, which includes both the Hα and continuuum emission integrated over the narrow wavelength range of our data. The circular boundary reflects the $\sim 8'$ field of view, and the gaps in the image are between CCD chips. (c) The total Hα intensity from line profile fits to our SALT Fabry-Pérot data. (d) The total H I intensity $\int Idv$ from the VLA.

~ 45 stars present in both the SALT and CTIO images to determine a smooth two-dimensional quadratic polynomial for each Fabry-Perot exposure that both corrects the residual flat field variations and normalizes the images to a common sensitivity. After correction, the stellar photometry in the Fabry-Perot images is accurate to 2 to 4% and is primarily limited by photon statistical noise in the narrow-band exposures.

3.3. *Line profile*

The transmission profile of the etalon as a function of wavelength is well-described by a Voigt function,

$$V(\lambda;\sigma,\gamma) = \int_{-\infty}^{\infty} G(\lambda';\sigma)L(\lambda-\lambda';\gamma)d\lambda', \qquad (1)$$

where $G(\lambda;\sigma)$ and $L(\lambda;\gamma)$ are Gaussian and Lorentzian distributions, respectively. For the medium resolution etalon used in these observations, there is significant degeneracy between the widths of the Gaussian and Lorentzian components, σ and γ. The instrumental profile is fitted well with the parameters $\sigma = 1.27$ Å and $\gamma = 1.02$ Å, giving a FWHM of 4.23 Å, or a velocity equivalent of 196 km s^{-1}.

3.4. *Wavelength measurements*

Since light that reaches different points in the image illuminates the etalon at different angles in the collimated beam, the wavelength of peak transmission varies over the image. The wavelength of peak transmission at a pixel is given by

$$\lambda_p(z,t,R) = \frac{\lambda_0(z,t)}{\sqrt{1+R^2/F^2}}, \qquad (2)$$

with

$$\lambda_0(z,t) = A + Bz + Et. \qquad (3)$$

Here z is a control parameter describing the spacing of the etalon plates, t is the time of the observation, R is the pixel's distance from the optical axis of the etalon, F is the focal length of the camera optics measured in units of image pixels, and λ_0 is the wavelength of peak transmission along the optical axis. As seen in equation (3), λ_0 varies linearly with z (we find no evidence for a more complicated dependence), and we also allow for a linear drift of λ_0 with t. The small fitted value $E \sim 2$ Å hr^{-1} is a measure of the stability of the instrument.

Across a single exposure, λ_p depends only on R. A uniformly illuminated, monochromatic source will therefore

be imaged as a ring centered on the optical axis of the etalon. This ring's intensity will be greatest at the radius $R_{\rm line}$ for which $\lambda_p(z, t, R_{\rm line}) = \lambda_{\rm line}$. Our 50 exposures of NGC 2280 contain several rings corresponding to night-sky emission lines of OH and [N II] (Osterbrock *et al.* 1996). We use these rings to calibrate the four coefficients A, B, E, and F. We fit a separate wavelength solution for each of the two nights of observations. Using ~ 15 imagings of 4 night-sky emission lines from each night, we fit the parameters A, B, E, and F such that the root mean square residual to our fit is minimized. The root mean square residuals for our two wavelength solutions are $\lambda_{\rm rms} = 0.159$ Å and $\lambda_{\rm rms} = 0.089$ Å for the 1 Nov 2011 and 28 Dec 2011 data respectively.

For the data taken on 1 Nov 2011, we find that the neon calibration lines systematically deviate from our best fit to the night-sky emission lines by ~ 3 Å and we therefore use only the night-sky lines to calibrate our wavelengths for that night. We do not understand the large discrepancy between night sky and calibration system lines, but similar differences have been found in other RSS FP data sets, and the current SALT calibration system is known to illuminate the telescope's spherical aberration corrector differently than does the primary mirror. The neon calibration lines from 28 Dec 2011 are consistent with the night-sky emission lines and we include both sets of lines in our wavelength solution for that night.

Once the night-sky emission lines have been used for wavelength calibration, they must be removed since they often overlap the image of NGC 2280. We compute a Voigt function centered around each line and map these functions onto our images by inverting equation (2). We then subtract these rings from our images, effectively removing the night-sky emission.

3.5. *Ghosts*

Reflections between the CCD detector and the Fabry-Perot etalon give rise to a ghost image, termed the "diametric ghost" in the discussion of Jones *et al.* (2002). This ghost image is in focus and is mirror-symmetric about the optical axis, with an amplitude of approximately 5-8%. The amplitude of the ghost image depends upon the quantum efficiency and reflectivity of the CCD, the etalon transmission and reflection profiles, the filter transmission curve, and the spectrum of the source; due to these complexities, the ghost amplitude varies over the image. We determine the precise position of the optical axis in our images by measuring the positions of ~ 20 bright stars and their ghosts. We rotate each image about this axis by 180°, scale by a factor of 0.065, and subtract this "ghost image" from the original. While this procedure overcorrects some stellar ghosts and undercorrects others by as much as 1.5%, it is effective at removing the reflection of the galaxy's core, where the ghost would most affect our measurements. We hope to implement calibration procedures in the future that will more accurately correct for the diametric ghost.

3.6. *Velocity measurements and uncertainties*

We use the measured centroids of ~ 35 stars present in our SALT data to align our images such that the same pixel corresponds to the same point on the sky in all 50 exposures. The precision of the individual stellar centroids is $\sim 0.1''$. The required shifts are $\sim 0.1''$ between

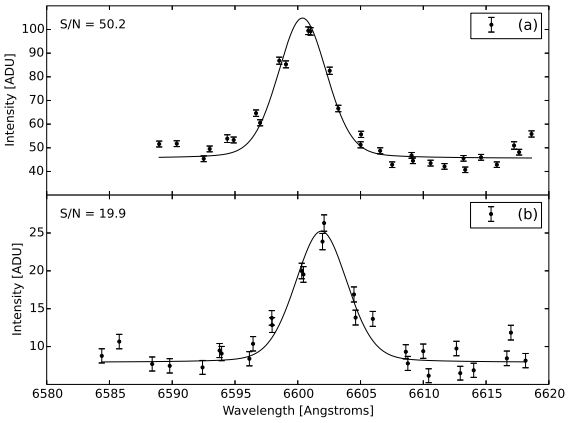


FIG. 2.— Sample spectra and Voigt profile fits to individual pixels in our Hα velocity map data. The pixels whose profiles are plotted here are marked in Figure 3.

images taken during a single night, but we also had to rotate our images from the second night by 110.85°.

In order to improve signal-to-noise (S/N), we employ a 9×9 pixel binning in each FP frame. Some groups (Cappellari & Copin 2003; Epinat *et al.* 2008) use Voronoi tesselation to combine low S/N pixels until the spectral line shift can be measured reliably. While this procedure indeed allows velocities to be fitted in regions where the line signal is weak, we have not adopted it here. The principal science goal of this study is to determine the rotation curve; adding more low S/N points to our maps will have very little effect on the fit, as the extra points will have low weight in the fit. Furthermore, the variable spatial resolution of such a map would greatly complicate the extraction of a rotation curve, as one should take into account the differing uncertainties in the locations of the measured velocities.

Once aligned, the data sets from the two nights were combined and fitted simultaneously. The combined series of images taken at different values of z provides a short piece of spectrum at every point. Etalon spacings were chosen such that the values of $\lambda_0(z, t)$ were spaced ~ 2 Å apart. We fit the spectrum at each pixel with a Voigt function to determine the wavelength of peak Hα emission and the uncertainty in that wavelength. In general, we fit for five parameters: the line strength I, the continuum strength I_0, the line center $\lambda_{\rm peak}$, the Gaussian width σ, and the Lorentzian width γ, together with uncertainty estimates in these values. We assume that the Hα emission profile is purely Gaussian, and the Lorentzian width γ is held fixed at the measured value from the neon calibrations. The wavelength $\lambda_{\rm peak}$ of peak emission and the uncertainty in determining this peak wavelength $\Delta\lambda_{\rm peak}$ are then used to calculate a velocity and velocity uncertainty for each pixel:

$$v = c(\lambda_{\rm peak} - \lambda_0)/\lambda_0 \quad (4)$$

$$\Delta v = c(\Delta\lambda_{\rm peak})/\lambda_{\rm peak} \quad (5)$$

Velocity uncertainties for pixels with strong Hα emission are typically ~ 3 km s^{-1}. We use the ratio of line strength to its uncertainty, $I/\Delta I$, as a proxy for S/N and discard velocity measurements from all pixels with values of $I/\Delta I < 5$ from our velocity map. We have ex-

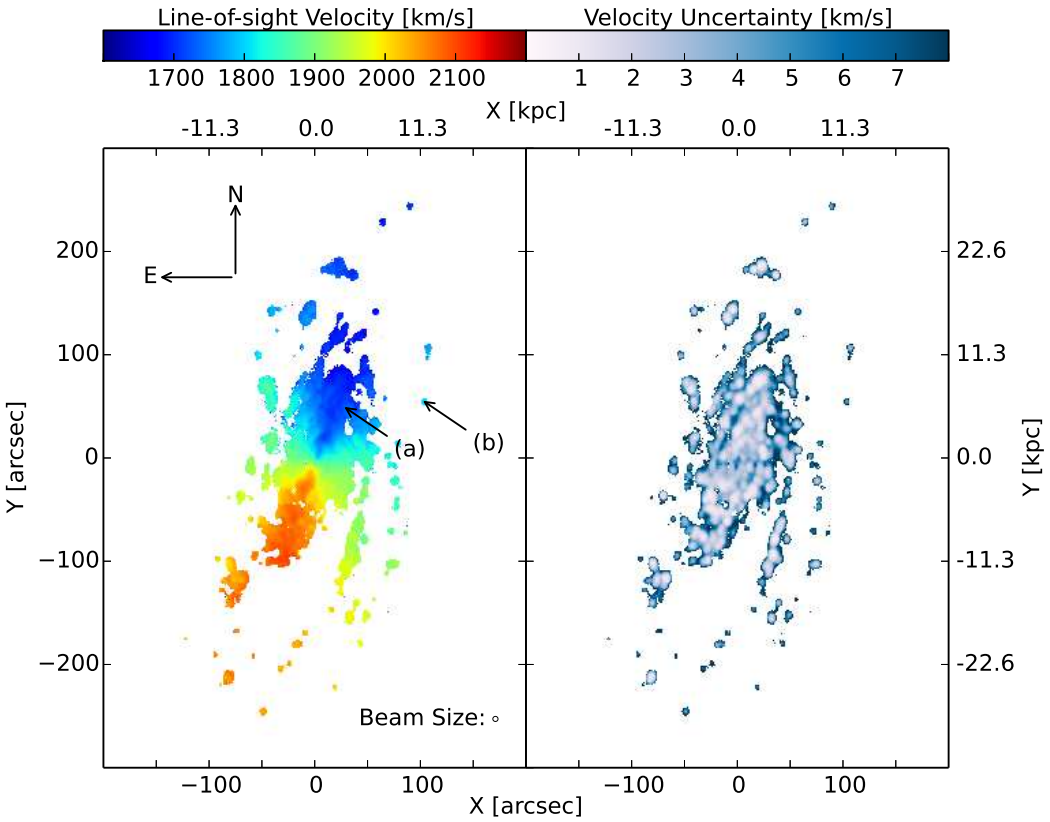


FIG. 3.— Velocity map (left) and velocity uncertainties (right) produced from the Hα data. The small circle in lower right corner of the velocity map represents the 4.9″effective beam size. Arrows indicate the pixels whose line profiles have been plotted in Figure 2.

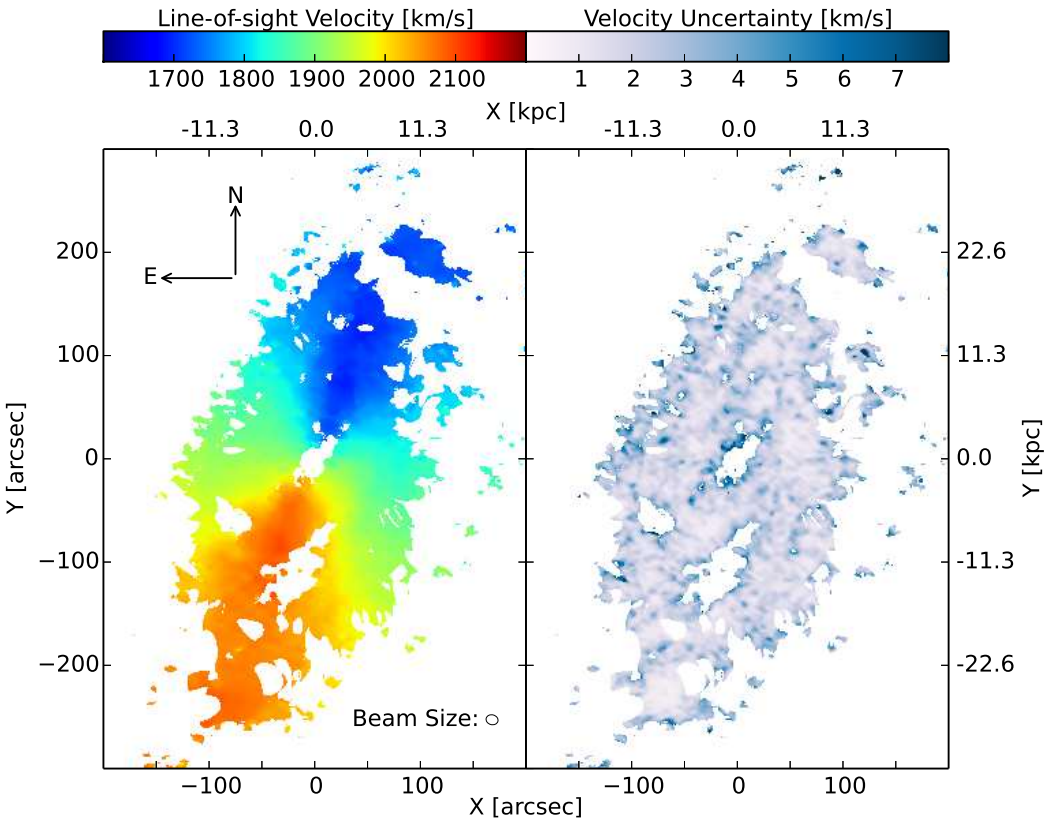


FIG. 4.— Velocity map (Left) and velocity uncertainties (Right) produced from the H I data.

TABLE 2
H I Observation Parameters

Parameter	Value
VLA configuration	BC
Synthetic beam FWHM	$11.46'' \times 9.54''$ at $74.39°$
Time on-source	370 minutes
Usable total bandwidth	2.5 MHz
Band center (helio)	1888 km s^{-1}
Spatial resolution	$10.46''$
Spatial resolution	1.18 kpc
RMS noise, H I line	0.47 mJy/beam

amined individual spectra of several hundred pixels and have found that they are each well-fitted by a single Voigt function. However, any possible spectral features such as multiple peaks that are more closely spaced than our spectral resolution 4 Å would be undetectable. Two sample spectra and Voigt profile fits for representative high and low S/N pixels are presented in Figure 2.

We also detect emission at 6583 Å from [N II] in NGC 2280, but as our wavelength coverage was not complete enough to capture the full line at all velocities, we are unable to produce a second velocity map from the [N II] data. However, where the line strength and wavelength coverage permitted, the fitted velocities using the [N II] line are consistent with those from the Hα line. When fitting the Hα line, we exclude wavelengths more than 13 Å redward of its peak so as to fit only the Hα emission and continuum.

Our Hα velocity map comprises $\sim 4.5 \times 10^4$ pixels which meet our S/N threshold of $I/\Delta I > 5$; of these 950 are completely independent. Figure 1(c) shows the distribution of Hα emission in NGC 2280.

The Hα velocity and uncertainty maps are shown in Figure 3. The velocity map is typical of a rotating circular flow pattern seen in projection, and the close spacing of the velocity contours near the center is indicative of a steep inner rise to the rotation curve. There is little evidence for a twist in the inner flow pattern, suggesting that any possible bar or oval distortion in the mass distribution is either very weak, or is aligned with the one of the principal projection axes.

The velocity field is well-sampled in the inner parts, but is increasingly sparsely sampled as the distance from the center approaches $200''$, or $\sim$ 25 kpc. The distribution of well-defined velocities for H II regions is not random and traces the spiral structure somewhat. Our 9×9 binning procedure to improve S/N gives a characteristic minimum size of $4.9''$ to the velocity "blobs", which is particularly apparent in the right panel of Figure 3, where the velocity uncertainty increases outward from the center of each blob as the S/N decreases.

4. H I OBSERVATIONS

Our H I observations were taken on 13 Oct 2006 using the VLA in BC configuration during the expansion phase of the array, which at the time contained five retro-fitted EVLA antennae. Other parameters of the observations are listed in Table 2. Standard flux calibrators, 3C147 and 3C286, were observed at the beginning and end of the observing run. A nearby phase calibrator, 0609-157, was observed for ∼4.5 minutes for every ∼30 minutes on the target source for a total of 370 minutes of on-source observing.

Data editing and reduction was completed using the Astronomical Image Processing System (AIPS) version 31Dec12 (Greisen 2003). Due to technical reports of power aliasing affecting the EVLA-EVLA baselines, all ten potentially affected baselines were flagged and removed from the data. The remaining data were then calibrated using standard AIPS tasks where the flux density for each source was determined relative to that of the flux calibrators and the phase of the data was retrieved from the computed phase closures from the phase calibrator. Bandpass solutions were also derived using the flux calibrators to correct for amplitude variation. The edited cube was imaged with robust weighting and cleaned, producing a synthesized beam FWHM of $11.46'' \times 9.54''$ at a position angle of 74.39°, a spectral resolution of 10.4 km s^{-1}, and an RMS noise in each spectral channel of $\sigma = 0.47$ mJy.

The differing spatial and spectral resolutions of our H I and FP data necessitate different approaches to extracting velocity maps. Velocity spreads across the beam, known as "beam smearing" (*e.g.,* Bosma 1981; Swaters *et al.* 2000), can give rise to aysmmetric line profiles that can be corrected for, to some extent, in the H I data with its higher spectral resolution. Beam smearing is less of a problem in higher spatial resolution optical data, but could not be corrected for in our data, as the instrumental broadening effectively hides any intrinsic asymmetry in the line profiles. We therefore adopt a different approach to extract the best possible velocity map from our H I data.

Figure 1(d) shows a map of the total H I intensity $\int Idv$ derived from the continuum-subtracted, calibrated data cube. Locations where $\int Idv < 6.4 \times 10^{20}$ atoms cm^{-2} before primary beam correction – the 3σ, 3-channel sensitivity limit of the cube – have been masked. We estimate velocities and uncertainties from a Hermite 3 fit (van der Marel & Franx 1993) following a similar approach to that described in Noordermeer *et al.* (2005) (see also de Blok *et al.* 2008). We use fits obtained from a smoothed and clipped version of the data cube as initial guesses in our fit to the full-resolution cube. The resulting Hermite 3 velocities are kept only for pixels where (a) the uncertainty on the best fitting velocity is $\sigma_V < 25$ km s^{-1}, (b) the peak of the Hermite 3 profile exceeds 3σ, (c) the velocity dispersion σ_d is in the range 5 km s^{-1} $< \sigma_d <$ 100 km s^{-1}, and (d) $\int Idv > 0$ in the intensity map of Figure 1.

Figure 4 shows the Hermite 3 velocity field and uncertainties for NGC 2280. As for Figure 3, the H I velocity map reveals a similar circular flow pattern, but with some differences. Velocities are determined over a wider region, with more complete coverage in the outer parts, but we were unable to obtain velocities in an elliptical region at the center that is extended roughly along the major axis. Even without data in this region, the inner velocity gradient appears shallower than in the Hα velocity map. The flow pattern is remarkably regular, with no clear twists in the iso-velocity contours, even in the outer parts, suggesting that any possible warp in the disk of NGC 2280 is mild and that the galaxy is undisturbed.

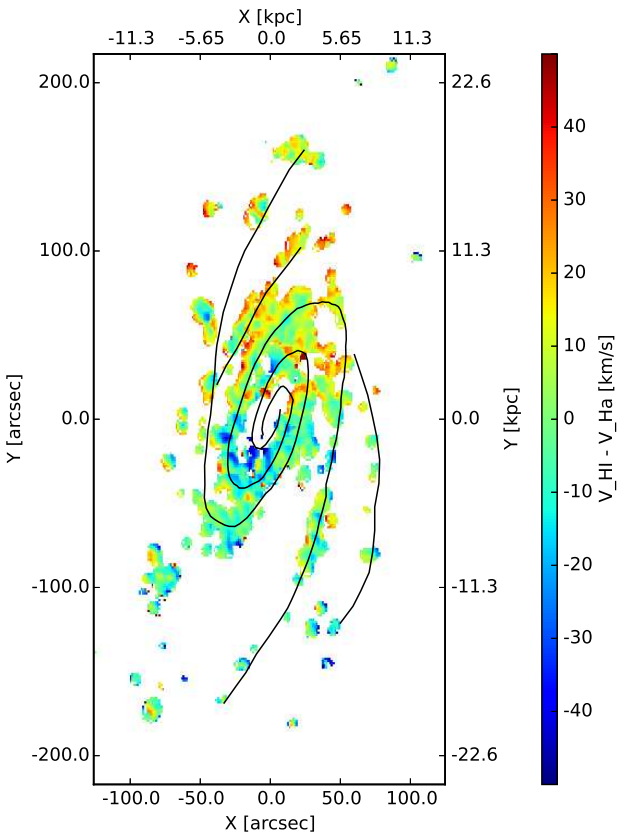


FIG. 5.— Differences in line-of-sight velocity between individual pixels in our Hα and H I velocity maps. The black lines show visually-estimated locations of the spiral arm features.

5. VELOCITY MAP COMPARISON

Figure 5 shows differences between the velocities in our Hα and H I velocity maps where both measurements are above our S/N thresholds. Differences are generally small (green color), but larger differences of $\gtrsim 40$ km s^{-1} are evident in some places and are not randomly distributed. In some parts, particularly in the north, positive differences (red) persist over regions that are azimuthally extended and there are hints that they could be associated with spiral features, shown by the black lines, although many red areas also lie squarely between arms. There are fewer differences $\lesssim -40$ km s^{-1} (blue) and they show essentially no correlation with spiral locations.

Note that a very few pixels have absolute velocity differences between the Hα gas and H I gas ranging up to ~ 200 km s^{-1}. This is not without precedent, Zánmar Sánchez *et al.* (2008) also noted a few H II regions in NGC 1365 having measured velocities that differed by $60-80$ km s^{-1} from that of the surounding gas and H I, and suggested they could be outside the plane and seen in projection.

While the loci of positive differences ~ 40 km s^{-1} do coincide with spiral arms in one or two instances, interpreting them as due to unusually strong spiral arm streaming makes little dynamical sense, for the following reason.

The NW side of the galaxy is approaching, which means that the NE side is tipped towards us if we assume the spirals trail. The difference map shows small velocity differences (green) that suddenly jump to ~ 40 km s^{-1} (red) on the NE sides of the spiral arms in one or two places in the N part of the map. The sign of the velocity difference ($v_{\rm H\,I} - v_{\rm H\alpha}$) implies that the H$\alpha$ emission is coming from gas that is moving, relative to that producing the H I line, towards us along our line of sight. Since the NE is the near side of the galaxy, this excited gas is therefore moving radially outwards from the center of the galaxy. (We discount the alternative possibility that the H I is moving away, since there are features in the Hα velocity maps at these locations that are not present in the H I map.) However, spiral streaming theory suggests that post-shock gas should have a component of velocity in towards the galaxy center inside corotation for the pattern. So either the spiral arms are outside corotation wherever this difference is seen, and the gas acquires its outward velocity *before* it passes through the arm, or the spirals are leading. Neither of these alternatives seem palatable.

Since the velocity differences are not well correlated with spiral arms, nor do they have the sign expected from spiral streaming theory where they do coincide with spirals, we suspect that they have some other origin. We note that similar patchy differences between $v_{\rm H\,I}$ and $v_{\rm H\alpha}$ were reported by Phookun *et al.* (1993) in the galaxy NGC 4254, for which they could find no convincing explanation.

We use the biweight (Beers *et al.* 1990) to estimate the Gaussian spread of the velocity differences. This estimator is designed to determine the spread from the bulk of the data without being biased by possible heavy tails in the distribution. Using the biweight, we find the mean velocity difference between our two maps to be $v_{\rm H\,I} - v_{\rm H\alpha} = 2.5$ km s^{-1} and the 1-σ scatter in these differences is 14.3 km s^{-1} about the mean. We find lower dispersions, 12.0 km s^{-1} for the approaching side only, and 11.9 km s^{-1} for the receding side, consistent with minor systematic differences for the two sides discussed below. These last two values are entirely consistent with intrinsic ISM turbulent motions of ~ 8.0 km s^{-1} Gunn *et al.* (1979), combined with a difference of two observed quantities with our (small) estimated uncertainties. Thus aside from the patchy large differences shown in Figure 5, our two velocity measurements in NGC 2280 generally differ by an amount that is no more than the usual expectation for turbulence in the ISM.

6. VELOCITY MAP FITTING

The *DiskFit*[5] software package (Spekkens & Sellwood 2007; Sellwood & Zánmar Sánchez 2010) is ideally suited for analysis of velocity maps such as ours. In its simplest version, the program constructs a model of a circular flow pattern in an inclined, thin, flat disk. It adjusts the circular speed at a specified set of radii, together with the systemic velocity, disk center, inclination and position angle of the entire disk, to find the values of these parameters that minimize the net χ^2 difference between the model flow and the velocity map. It is also capable of fitting non-circular flow patterns caused by bars, or radial variations to the projection angles caused by

[5] *DiskFit* is publicly available for download at http://www.physics.rutgers.edu/∼spekkens/diskfit/

warps. Unlike other methods, it therefore utilizes all the data in the entire map to constrain the projection geometry, and uses a bootstrap technique to yield meaningful uncertainties in all the fitted parameters.

We have employed this software to fit our Hα and H I velocity maps of NGC 2280. For each of our two velocity maps, we fit two separate models: one for which the position angle, ellipticity, and center were free to vary, and the other with these parameters held fixed at common values so that we can directly compare the fitted rotation curves. Our first fits are of simple disk models without bars or warps.

The measurement uncertainties needed to estimate χ^2 for the fit are the Δv found when fitting the Hα and H I lines. Since the emission we observe may not be coming from matter traveling at the circular speed, we add an additional 8 km s^{-1} in quadrature to the uncertainties in both velocity maps. This value is typical of turbulent motions in the interstellar medium of a galaxy (Gunn *et al.* 1979) and roughly that estimated above from the scatter in the differences between our two velocity maps in Figure 5.

6.1. *Projection parameters*

Table 3 gives the fitted values, together with our estimated uncertainties, of the projection parameters from the two maps separately. The two estimates of the systemic velocity differ by 1.8 km s^{-1}, which is well within the quoted 1-σ uncertainties. Our values are smaller than those quoted by Koribalski *et al.* (2004) and by Springob *et al.* (2005). Because our systemic velocity was derived from 2-D velocity maps and theirs from a single-dish H I measurements, we do not find this difference worrisome.

Our kinematic estimates of the position angle and ellipticity from our two maps are also in excellent agreement with each other, and agree tolerably well with previous apparent ellipticity ($e = 1 - b/a$) estimates from a photometric B-band image (Lauberts & Valentijn 1989) and from 2MASS near-infrared data (Jarrett *et al.* 2003) given in Table 3. Mild discrepancies between photometric and kinematic estimates of inclination can arise from intrinsic mild ellipticities caused by outer spiral arms, for example. Our favored values for the parameters in Table 3 were determined by weighted means of our two best fitting models, with weights given by the inverse variances of these quantities.

6.2. *Uncertainty estimates*

Figures 6 and 7 show respectively our best fitting rotation-only models for both the Hα and H I velocity maps and the corresponding residual maps. The values of the reduced χ^2 for these models are 2.33 and 1.75 respectively, indicating a poor formal fit to the data. The residual velocities are significantly larger than our typical velocity uncertainties, which are usually dominated by our adopted value of 8 km s^{-1} for turbulent motions in the ISM, and are generally spatially correlated, indicating that the gas in NGC 2280 has more complicated motion than is allowed for in our models. For example, our models do not include non-circular streaming motions associated with spiral arms. A dynamical origin for the larger residuals is supported by the fact that their general pattern is similar in the two separate datasets.

The *DiskFit* program is capabale of fitting a bar flow pattern of any amplitude and/or a crude model for a warp. We have attempted to fit our velocity maps with models that include bars or warps, but find that the inclusion of these features does not substantially improve the fits. However, *DiskFit* does not have the capability to fit more complicated spiral streaming patterns, which are generally less clearly rotationally symmetric than are bars and probably arise from superposed multiple spiral modes (Sellwood & Carlberg 2014). Since we are unable to model these features in our data, we must assess the extent to which their presence affects the values of our derived quantities.

The usual bootstrap technique adds randomly rearranged residuals at every pixel to the best-fit model to create many pseudo-data sets, and determines uncertainties in the parameters from their scatter in fits to the pseudo-maps. This approach assumes that the residuals from the original fit are uncorrelated and, were we to apply it in our case, it would destroy the correlated nature of the residuals and lead to uncertainty estimates that would be far too small. *DiskFit* therefore offers two distinct methods to retain the correlated nature of the residuals: since we see that the residuals reflect a spiral flow pattern, we utilize the method developed by Sellwood & Zánmar Sánchez (2010). Our uncertainties are estimated from 1000 bootstrap iterations.

6.3. *Rotation curve*

Figure 8 shows the circular speed derived from our fits to the Hα and H I velocity maps, with the error bars showing $\pm 1\sigma$ uncertainties. The abscissae were chosen such that the points are spaced 1 beam FWHM apart.

We have also fitted models to the approaching and receding halves of the galaxy independently. For these models, we fit only points which are north or south of the minor axis, respectively, and we fix the systemic velocity, position angle, and ellipticity to the favored values listed in Table 3. In Figure 9, we show rotation curves derived from these models to both the Hα and H I velocity data. We note that the rotation curves produced from these models are largely consistent with each other. The extreme outlying points in the approaching Hα curve are determined by very few pixels that are far from the major axis, and thus are sensitive to deprojection errors. There are some asymmetries in the estimated speeds that are most pronounced over the range $30'' < r < 100''$. For both the Hα and H I velocity maps, the receding side of the galaxy appears to have a slightly higher rotational speed at these radii than does the approaching side. Asymmetries in these fitted speeds are probably caused by $m = 1$ distortions in the galaxy, although $m = 3$ could not be ruled out. Their presence is somewhat surprising in a galaxy that seems so undisturbed and hosts such a regular bi-symmetric spiral pattern.

The combined Hα rotation curve (Figure 8) manifests a series of small "bumps" that are less prominent or nonexistent in the H I rotation curve. These bumps stand out more clearly on the approaching side (blue circles in Figure 9), while the rotation curve is smoother on the receding side. They are almost certainly related to the large velocity differences visible in Figure 5, which revealed patches of excited gas moving more rapidly towards us (red) on the approaching side (north west),

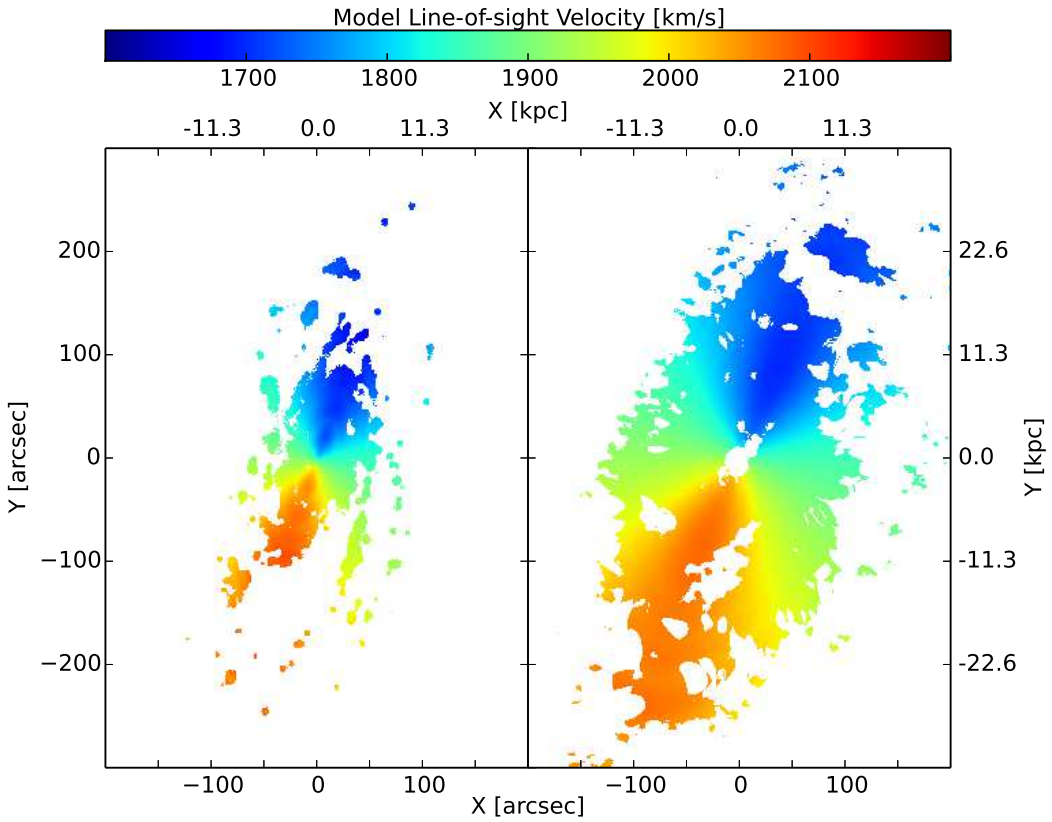


FIG. 6.— Best fitting models to the Hα (Left) and H I (Right) velocity maps.

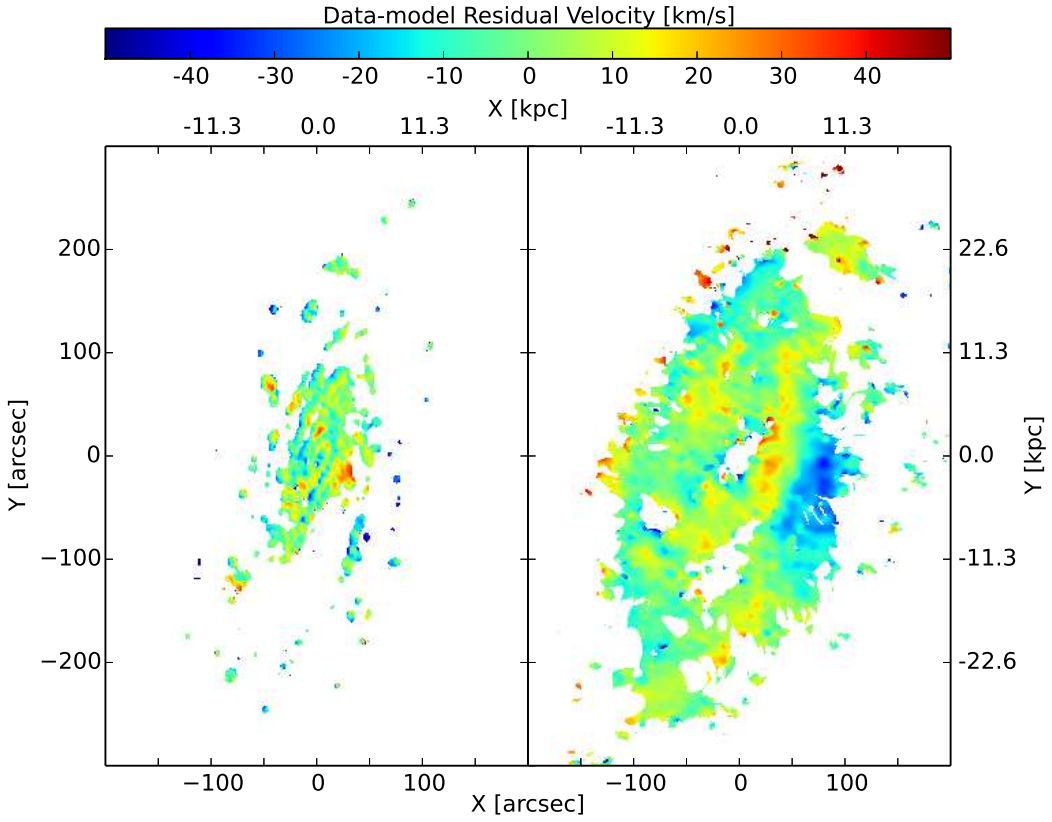


FIG. 7.— Data-model residuals for the best fitting models to the Hα (Left) and H I (Right) velocity map.

TABLE 3
SUMMARY OF NGC 2280 PROPERTIES

Property	Previous Work	Hα Measurements	H I Measurements	Favored Values
Position Angle	$163°$[a] / $155°$[b]	$157.9 \pm 0.5°$	$157.4 \pm 0.5°$	$157.7 \pm 0.4°$
Ellipticity	0.56[a] / 0.59[b]	0.57 ± 0.02	0.55 ± 0.02	0.55 ± 0.01
Center Right Ascension	6h44m49.11s±0.08s[c]	6h44m49.09s±0.02s	6h44m49.03s±0.07s	6h44m49.09s±0.02s
Center Declination	-27°38′19.0″±1.25″[c]	-27°38′17.7″±0.5″	-27°38′16.2″±0.9″	-27°38′17.4″±0.4″
Systemic Velocity (helio)	1895 ± 1 km s^{-1}[d]	1887 ± 2 km s^{-1}	1888 ± 1 km s^{-1}	1888 ± 1 km s^{-1}
(cont.)	1899 ± 3 km s^{-1}[e]			
(cont.)	1905 ± 6 km s^{-1}[f]			
(cont.)	2041 ± 8 km s^{-1}[g]			

NOTE. — A comparison of the previously measured properties of NGC 2280 to the properties measured from our best fitting Hα and H I velocity map models and our favored values. Ellipticities from previous works were derived from the major and minor axis measurements in those works.

[a] Lauberts & Valentijn (1989) from optical photometry
[b] Jarrett *et al.* (2003) from 2MASS K_s photometry
[c] Skrutskie *et al.* (2006)
[d] Springob *et al.* (2005) from H I spectrum
[e] Koribalski *et al.* (2004) from H I spectrum
[f] Bottinelli (1990) from H I spectrum
[g] Sandage (1978) from optical spectrum

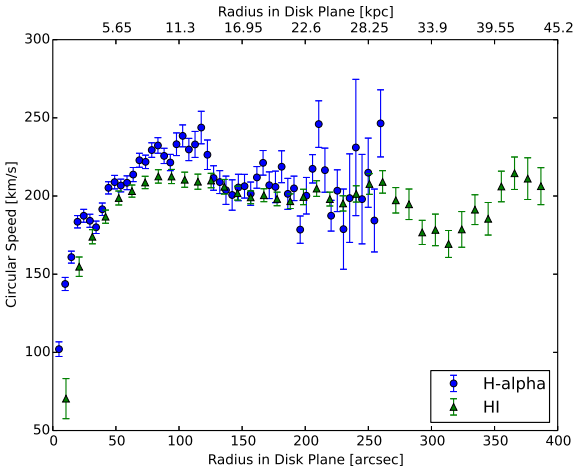


FIG. 8.— Rotation curves for NGC 2280 derived from the model fits to our Hα and H I data.

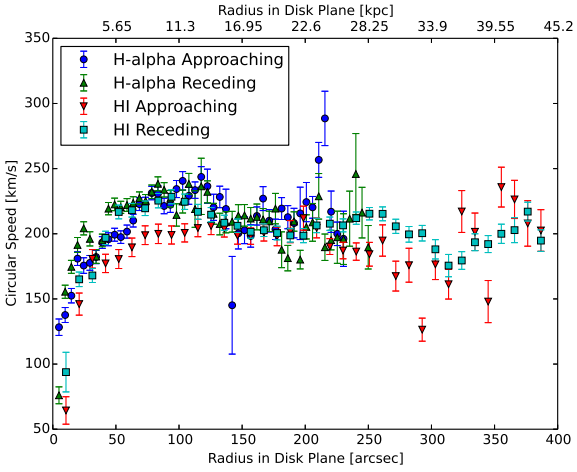


FIG. 9.— Rotation curves for NGC 2280 produced from independent model fits to the approachingand receding halves of our Hα and H I data.

while there are fewer anomalous velocties on receding side. The origin of these kinematic differences between the excited and neutral gas in NGC 2280 is unclear at this point.

Aside from these anomalous Hα velocities, the rotation curves derived from our two maps appear to be in reasonable agreement with each other, and most differences stem from the different spatial coverage and resolutions of the separate maps, which complement each other well. As shown in Figures 3 and 4, the Hα velocity map is more sparsely sampled at large radii than is the H I velocity map, leading to larger fluctuations and greater residuals in the optically estimated circular speed (Figure 8). However, the inner rise of the rotation curve is better resolved in the optical data, as we discuss in more detail next.

6.4. *Inner velocity gradient*

The slope of the inner rise of the H I circular speed is shallower than that found from the optical data. One well-known reason for the shallower central gradient from

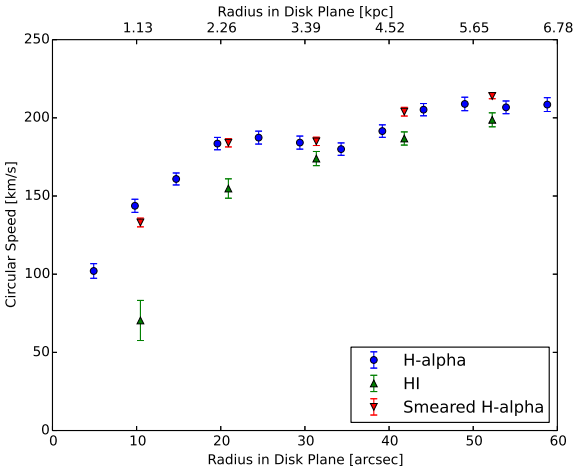


FIG. 10.— Inner rise of rotation curves derived from the model fits to our unsmeared Hα, H I, and Hα smeared to the resolution of the H I data.

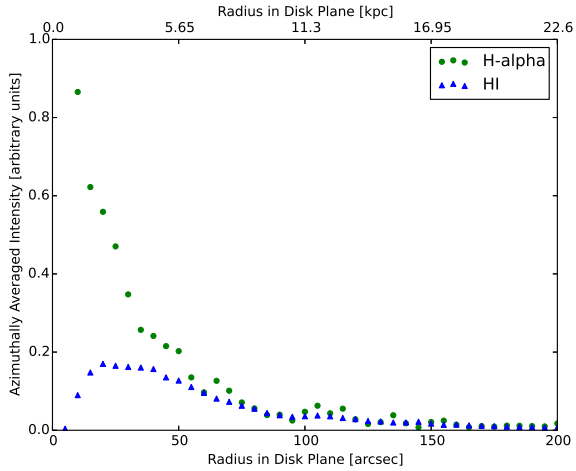


FIG. 11.— Azimuthally averaged intensity profiles of NGC 2280 from our Hα and H I data, in 5″ radius bins. Note the central hole in the H I intensty profile that is not present in the Hα profile.

the H I measurements is beam smearing (Bosma 1981; Swaters *et al.* 2000), which has the effect of combining velocities of gas away from the major axis with those from gas on the major axis. Since projection causes the line-of-sight velocity to be systematically smaller away from the major axis, beam smearing always biases rotational velocity measurements towards lower values.

In order to determine whether spatial resolution alone is responsible for the different central gradients, we have convolved our FP data with a Gaussian beam identical to that used for the H I data. This procedure required us first to take out the center-to-edge velocity gradient in the FP frames in order to make a new data cube with single velocity "channels" before blurring. We then modelled the resulting velocity map with the *DiskFit* software. In Figure 10, we plot the inner rise of rotation curves for our unsmeared Hα (blue circles), smeared Hα (red inverted triangles), and H I data (green triangles). As expected, the beam smeared Hα rotation curve has a shallower rise inside $R = 20''$ than that of the unsmeared

Hα rotation curve.

However, the beam smeared Hα rotation curve still rises more steeply than does the H I rotation curve, although the H I data are sparse within $\sim 30''$ of the galaxy center. We attribute the yet shallower rise to a deficiency of H I emission in the center of NGC 2280. Figure 11 shows the azimuthally averaged intensity profiles for the Hα and H I data. The H I surface density drops toward the center, consistent with the $\sim 30''$ central hole in the intensity map (Figure 1), a common feature of H I emission near the center of galaxies (*e.g.,* Wang *et al.* 2014).

The weak H I line cannot yield reliable velocities, whereas the Hα intensity rises continuously into the center enabling reliable velocity measurements at small radii. This difference in the radial distribution is probably responsible for the remaining difference between the rotation curves. Note that there must be some hydrogen in the center to produce the Hα emission, and the neutral gas is probably molecular therefore; however, we have been unable to find any existing CO observations to confirm the presence of molecular gas.

7. SUMMARY

We have presented detailed velocity maps of the nearby spiral galaxy NGC 2280 produced from Fabry-Pérot measurements of the Hα line of excited gas and from aperture synthesis measurements of the 21cm line of H I. Despite the fact that these two maps were derived from different components of the ISM having different spatial distributions, and were measured with different instruments having widely differing spatial and spectral resolutions, the measured velocities are generally in excellent agreement.

The kinematic maps of NGC 2280 reveal a remarkably regular flow pattern, with no evidence for a bar or oval distortion, or for a warp. In particular, the galaxy appears to be undisturbed, despite the presence of numerous, possibly-close companions listed in Table 1. We have obtained estimates of the systemic velocity, disk inclination and position angle using *DiskFit*. Our derived values from the two maps agree within their estimated uncertainties and we favor $\phi_{\rm PA} = 157.7 \pm 0.4°$, $e = 0.55 \pm 0.01$, and $v_{\rm sys} = 1888 \pm 1$ km s^{-1}. These values are broadly consistent with previous estimates, as shown in Table 3.

Additionally, the two datasets yield similar rotation curves. The differences in spatial extent and resolution between the Hα and H I velocity maps demonstrate the complementarity of the measurements. At small radii, the resolution of the Hα velocity map allows for a more precise measurement of the inner slope of the rotation curve. The better-filled velocity map from the H I allows us to measure the rotation curve to large radii with greater precision than could be obtained from the Hα velocity map.

We have compared the velocities from the two datasets at overlapping pixels, and find a near Gaussian spread of differences with a dispersion of ~ 14 km s^{-1}, consistent with an intrinsic velocity dipersion of ~ 8 km s^{-1} broadened by the combined uncertainties from measurements by the two instruments. However, a small fraction of the pixels manifest much larger differences, $\gtrsim \pm 40$ km s^{-1}, whose origin is unclear.

Future papers in this series will present both optical and 21 cm velocity maps and deep optical photometry of all 19 galaxies in our RINGS survey. Our ultimate goal is to fit these data with mass models in order to constrain the radial distibution of dark matter in each galaxy and to compare that with predictions from ΛCDM cosmology.

We thank Tad Pryor for many helpful conversations about the intricacies of Fabry-Pérot data reduction and the referee for a detailed report. This work was supported by NSF grant AST-1211793 to JAS and TBW. TBW acknowledges support by the National Research Foundation of South Africa under grant CSUR87704. KS acknowledges support from the Natural Sciences and Engineering Research Council of Canada (NSERC). This research has made use of the NASA/IPAC Extragalactic Database (NED) which is operated by the Jet Propulsion Laboratory, California Institute of Technology, under contract with the National Aeronautics and Space Administration.

REFERENCES

Arp, H. C. & Madore, B. F. 1987, "A Catalogue of Southern Peculiar Galaxies and Associations" (Cambridge, UK: Cambridge University Press)
Athanassoula, E., Bosma, A. & Papaioannou, S. 1987, A&A, **179**, 23
Babcock, H. W. 1939, Lick Observatory bulletin, **19**, 41
Beers, T. C., Flynn, K. & Gebhardt, K. 1990, AJ, **100**, 32
Bershady, M. A., Martinsson, T. P. K., Verheijen, M. A. W., Westfall, K. B., Andersen, D. R. & Swaters, R. A. 2011, ApJL, **739**, L47
Bershady, M. A., Verheijen, M. A. W., Swaters, R. A., Andersen, D. R., Westfall, K. B. & Martinsson, T. 2010, ApJ, **716**, 198
Blumenthal, G. R., Faber, S. M., Flores, R. & Primack, J. R. 1986, ApJ, **301**, 27
Bosma, A. 1981, AJ, 86, 1791
Bottinelli, L., Gouguenheim, L., Fouque, P. & Paturel, G. 1990, A&AS, **82**, 391
Brook, C. B., Governato, F., Roškar, R., et al. 2011, MNRAS, **415**, 1051
Buckley, D. A. H., Charles, P. A., Nordsieck, K. H. & O'Donoghue, D. 2006, IAUS, 232, 1
Cappellari, M. & Copin, Y. 2003, MNRAS, **342**, 345
Condon, J. J., Helou, G., Sanders, D. B. & Soifer, B. T. 1996, ApJS, **103**, 81
Debattista, V. P. & Sellwood, J. A. 2000, ApJ, **543**, 704
de Blok, W. J. G., Walter, F., Brinks, E., Trachternach, C., Oh, S.-H. & Kennicutt, R. C. 2008, AJ, **136**, 2648
Dekel, A. & Birnboim, Y. 2006, MNRAS, **368**, 2
de Vaucouleurs, G., de Vaucouleurs, A., Corwin, H. G., Jr., Buta, R. J., Paturel, G., & Fouqué, P. 1991, Third Reference Catalogue of Bright Galaxies (New York: Springer)
Di Cintio, A. +2014, MN 437, 415
Dutton, A. A. *et al.* 2007, ApJ, **654**, 27
Einasto J. & Haud U., 1989, A&A, **223**, 89
Epinat, B., Amram, P., Marcelin, M., et al. 2008, MNRAS, **388**, 500
Fall, S. M. & Efstathiou, G. 1980, MNRAS, **193**, 189
Gao, L., *et al.*, 2008, MNRAS, **387**, 536
Garcia, A. M., Bottinelli, L., Garnier, R., Gouguenheim, L. & Paturel, G. 1994, A&AS, **107**, 265
Gnedin, O. Y., Kravtsov, A. V., Klypin, A. A. & Nagai, D. 2004, ApJ, **616**, 16
Governato, F., Brook, C., Mayer, L., et al. 2010, Natur, **463**, 203
Governato, F., Zolotov, A., Pontzen, A., et al. 2012, MNRAS, **422**, 1231
Greisen, E. W. 2003, Information Handling in Astronomy - Historical Vistas, 285, 109

Guedes, J., Callegari, S., Madau, P. & Mayer, L. 2011, ApJ, **742**, 76
Gunn, J. E. 1982, in *Astrophysical Cosmology*, eds. H. A. Brück, G. V. Coyne & M. S. Longair (Vatican City: Pontificia Academia Scientiarum) p. 233
Gunn, J. E., Knapp, G. R., & Tremaine, S. D. 1979, AJ, **84**, 1181
Hayashi, E. & Navarro, J. 2006, MNRAS, **373**, 1117
Hernandez, O., Carignan, C., Amram, P., Chemin, L. & Daigle, O. 2005, MNRAS, **360**, 1201
Hernandez, O., Fathi, K., Carignan, C., et al. 2008, PASP, **120**, 665
Huchra, J. P., Macri, L. M., Masters, K. L., et al. 2012, ApJS, **199**, 26
Jarrett, T. H, Chester, T., Cutri, R., Schneider, S. E. & Huchra, J. P. 2003, AJ, **125**, 525
Jones, D. H., Shopbell, P. L. & Bland-Hawthorn, J. 2002, MNRAS, **329**, 759
Kereš, D., Katz, N., Weinberg, D. H. & Davé, R. 2005, MNRAS, **363**, 2
Koribalski, B. S., Staveley-Smith, L., Kilborn, V. A., et al. 2004, AJ, **128**, 16
Kuzio de Naray, R. & Spekkens, K. 2011, ApJL, **741**, L29
Lauberts, A. & Valentijn, E. A. 1989, "The surface photometry catalogue of the ESO-Uppsala galaxies" (Garching: European Southern Observatory)
Matthews, L. D., Gallagher, III, J. S., & Littleton, J. E. 1995, AJ, **110**, 581
McGaugh, S. S., de Blok, W. J. G., Schombert, J. M., Kuzio de Naray, R. & Kim, J. H. 2007, ApJ, **659**, 149
Merritt D., Navarro J. F., Ludlow A. & Jenkins A. 2005, ApJ, **624**, L85
Navarro J. F., Hayashi E., Power C., et al. 2004, MNRAS, **349**, 1039
Navarro J. F., Ludlow A., Springel V., et al. 2010, MNRAS, **402**, 21
Navarro, J. F., Frenk, C. S. & White, S. D. M. 1996, ApJ, **462**, 563
Noordermeer, E., van der Hulst, J. M., Sancisi, R., Swaters, R. A. & van Albada, T. S. 2005, A&A, **442**, 137
Oh, S.-H., Brook, C., Governato, F., et al. 2011, AJ, **142**, 24
Öpik, E. 1922, ApJ, **55**, 406
Osterbrock, D. E., Fulbright, J. P., Martel, A. R., Keane, M. J., Trager, S. C. & Basri, G. 1996, PASP, **108**, 277
Paturel, G., Vauglin, I., Petit, C., Borsenberger, J., Epchtein, N., Fouqu, P. & Mamon, G. 2005, A&A, **430**, 751
Phookun, B., Vogel, S. & Mundy, L. G. 1993, ApJ, **418**, 113
Pontzen, A. & Governato, F. 2012, MNRAS, **421**, 3464
Pontzen, A. & Governato, F. 2014, Natur, **506**, 171
Rangwala, N., Williams, T. B., Pietraszewski, C. & Joseph, C. L. 2008, AJ, **135**, 1825
Read, J. I. & Gilmore, G. 2005, MNRAS, **356**, 107
Rhee, G., Valenzuela, O., Klypin, A., Holtzman, J. & Moorthy, B. 2004, ApJ, **617**, 1059
Roberts, M. S. 1969, AJ, **74**, 859
Rubin, V. C., Ford, W. K. & Thonnard, N. 1980, ApJ, **238**, 471
Sackett, P. D. 1997, ApJ, **483**, 103
Sandage, A. 1978, AJ, **83**, 904
Schommer, R. A., Bothun, G. D., Williams, T. B., Mould, J. R. 1993, AJ, **105**, 97
Sebring, T. A. & Ramsey, L. W. 1997, SPIE, 2871, 32
Sellwood, J. A. & Carlberg, R. G. 1984, ApJ, **282**, 61
Sellwood, J. A. & Carlberg, R. G. 2014, ApJ, **785**, 137
Sellwood, J. A. & McGaugh, S. S. 2005, ApJ, **634**, 70
Sellwood, J. A. & Zánmar Sánchez, R. 2010, MNRAS, **404**, 1733
Shetty, R., Vogel, S. N., Ostriker, E. C. & Teuben, P. J. 2007, ApJ, **665**, 1138
Skrutskie, M. F., Cutri, R. M., Stiening, R., et al. 2006, AJ, **131**, 1163
Spekkens, K. & Sellwood, J. A. 2007, ApJ, **664**, 204
Springel, V., Frenk, C. S. & White, S. D. M. 2006, Natur, **440**, 1137
Springob, C. M., Haynes, M. P., Giovanelli, R. & Kent, B. R. 2005, ApJS, **160**, 149
Swaters, R. A., Madore, B. F. & Trewhella, M. 2000, ApJL, **531**, L107
Tully, R. B. & Fisher, J. R. 1977, A&A, **54**, 661
Valenzuela, O., Rhee, G., Klypin, A., Governato, F., Stinson, G., Quinn, T. & Wadsley, J. 2007, ApJ, **657**, 773
van Albada, T. S., Bahcall, J. N., Begeman, K. & Sancisi, R. 1985, ApJ, **295**, 305
van der Marel, R. P. & Franx, M. 1993, ApJ, 407, 525
Wang, J., Fu, J., Aumer, M., et al. 2014, MNRAS, **441**, 2159
Weiner, B. J., Sellwood, J. A. & Williams, T. B. 2001, ApJ, **546**, 931
White, S. D. M. & Rees, M. J. 1978, MNRAS, **183**, 341
Zánmar Sánchez, R., Sellwood, J. A., Weiner B. J. & Williams, T. B. 2008, ApJ, **674**, 797